Spectral attenuation of gravity wave and model calibration in pack ice

Sukun Cheng[1,4], Justin Stopa[2], Fabrice Ardhuin[3] and Hayley H. Shen[4]

[1]Nansen Environmental and Remote Sensing Center, Bergen, Norway

5   [2]Department of Ocean and Resources Engineering, University of Hawaii, Mānoa, HI, USA

[3]Univ. Brest, CNRS, IRD, Ifremer, Laboratoire d'Océanographie Physique et Spatiale (LOPS), IUEM, Brest, France

[4]Department of Civil and Environmental Engineering, Clarkson University, Potsdam, NY, USA

Correspondence to: Sukun Cheng (sukun.cheng@nersc.no)

10   Three key points:

1. The spatial distribution of wavenumber and spectral attenuation in pack ice are analyzed from SAR retrieved gravity wave spectra.

2. Spectral attenuation rate of 9~15s waves varies around 10^{-5}m^2/s, with lower values in thicker semi-continuous ice field with leads.

15   3. The calibrated viscoelastic parameters are greater than those found in pancake ice.

Abstract. We investigate an instance of wave propagation in the fall of 2015 in thin pack ice (<0.3 m) and use the resulting attenuation data to calibrate two viscoelastic wave-in-ice models that describe wave evolution. The study domain is 400 km by 300 km adjacent to a marginal ice zone (MIZ) in the Beaufort Sea. From Sentinel-1A synthetic aperture radar (SAR) imagery, the ice cover is divided into two regions

20   delineated by the first appearance of leads. According to the quality of SAR retrievals, we focus on a range of wavenumbers corresponding to 9~15 s waves from the open water dispersion relation. By pairing directional wave spectra from different locations, we obtain wavenumber-dependent attenuation rates, which slightly increase with increasing wavenumber before the first appearance of leads and become lower and more uniform against wavenumber in thicker ice after that. The results are used to calibrate two viscoelastic

25   wave-in-ice models through optimization. For the Wang and Shen (2010) model, the calibrated equivalent shear modulus and viscosity of the pack ice are roughly one order of magnitude greater than that in grease/pancake ice reported in Cheng et al. (2017). These parameters obtained for the extended Fox and Squire model are much larger than laboratory values, as found in Mosig et al. (2015) using data from the Antarctic MIZ. This study shows a promising way of using remote sensing data with large areal coverage to

30   conduct model calibration for various types of ice cover.

KEY WORDS: pack ice, linear surface gravity wave, SAR derived wave spectra, wave attenuation, viscoelastic model calibration

1 Introduction

The rapid reduction of Arctic ice in recent decades has become a focal point in climate change discussions.

35   The fact that this reduction exceeds model predictions (Stroeve et al., 2007; Comiso et al., 2008) emphasizes the need to better understand the complex interaction between the sea ice, the ocean, and the atmosphere. One of these interaction processes is between ocean waves and sea ice. Ocean waves help to shape the formation of new ice covers (Lange et al., 1989; Shen et al., 2001), break existing ice covers (Kohout et al., 2016), modify the upper ocean mixing (Smith et al., 2018), or potentially compress sea ice through wave

40   radiation stress (Stopa et al., 2018a). In turn, ice covers alter the wave dispersion and attenuation, redistribute wave energy, suppress wave-wind interaction and wave breaking (Squire, 2007, 2018).

   To account for the ice effects in wave propagation, the spectral wave model WAVEWATCH III® (WW3) has included several dispersion/dissipation (IC0, IC1, IC2, IC3, IC4, and IC5) and scattering (IS1 and IS2) parameterizations, called "switches" in WW3, to estimate the ice effect on waves (WAVEWATCH III®

45   Development Group, 2019). Both IC3 and IC5 theorize that sea ice can store and dissipate mechanical energy, hence they model the ice cover as a viscoelastic material. Therefore, the energy dissipates and the dispersion changes when waves propagate through an ice field. The storage property is reflected in the potential and elastic energy, and the dissipative property is in the equivalent viscous damping. The difference between IC3 and IC5 is that IC3 is an extension of the viscous ice layer model with a finite thickness (Keller, 1998) by

50   including elasticity into a complex viscosity (Wang and Shen, 2010), while IC5 is an extension of the thin elastic plate model (Fox and Squire, 1994) introduced by Mosig et al. (2015) by adding viscosity into a complex shear modulus (equivalent to the complex viscosity via the Voigt model). Below we will refer to these two viscoelastic models as WS and FS respectively.

   To use these models for wave forecasts in ice-covered seas, one needs to determine these equivalent elasticity

55   and equivalent viscosity for all types of ice covers. To derive these parameters using first principles is challenging, as demonstrated by de Carolis et al. (2005), who obtained the viscosity of grease ice using principles in fluid mechanics of a suspension. Alternatively, an inverse method has been adopted to parameterize IC3. Using in-situ data from the R/V Sikuliaq field experiment (Thomson et al., 2018), the WS model was calibrated to match the observed wavenumber and attenuation (Cheng et al., 2017). This

60   calibration was carried out in a MIZ populated predominantly with grease/pancake ice. Although it showed good agreement between the calibrated model and the field data in the frequency band containing most of the wave energy, these calibrated values are limited to the grease/pancake ice type. Further into the ice cover, where more rigid ice with larger floes is present, how the equivalent viscoelastic parameters might change is unknown at present. Note the models will only be as robust as the training data. Therefore, the wider types

65   of sea ice that models have been trained will result in a more robust model.

   Advancements made in remote sensing technology have provided opportunities for such model calibration. During the R/V Sikuliaq experiment, the Sentinel-1A equipped with a synthetic aperture radar (SAR) acquired six sequential images around 16:50 UTC on 12 October 2015. These SAR images covered a 400 km by 1,100 km region including open water, grease/pancake ice, and pack ice (refer to Figure 1 in Stopa et

70   al. (2018b)). A large wave event during this time with wave heights exceeding 4 m in the captured region provided quality wave data. Ardhuin et al. (2017) developed a method to invert from wave orbital motion to directional wave spectra from SAR images of waves in sea ice based on the velocity bunching mechanism. Stopa et al. (2018b) refined this methodology for the partially and fully ice-covered regions by substantially reducing data contaminated by ice features with similar length scale as the wavelength. Using SAR retrieved

75   wave spectra, the authors found the significant wave height attenuated steeply prior to the first appearance of ice leads (denoted as FAL hereafter), with milder attenuation rate after the FAL.

An overview of ice and wave condition with available observations in the studied region is presented in Figure 1. More details of the retrievals are given in Stopa et al. (2018b). Significant spatial variability is observed in both the wave and ice conditions. Figure 1(a) presents a subregion captured by the SAR images

80   covering from a portion of Alaska to the largest azimuth position where waves are last observed visually in the images. Colors indicate the dominant wavenumber distribution of the retrievals, and arrows indicate the dominant wave direction defined in section 2. Cell size is coarsened to 12.5 km × 12.5 km to enhance visualization. The ice edge is indicated by the contours of ice concentration (<0.4) from AMSR2 (Advanced Microwave Scanning Radiometer 2, http://doi.org/10.5067/AMSR2/A2_SI12_NRT). An in-situ buoy:

85   AWAC-I (a subsurface Nortek Acoustic Wave and Current buoy, moored at 150ºW, 75ºN) is marked by a black asterisk. Except for the in-situ observations from the Sikuliaq ship (green diamond) and several drifting buoys (blue dots) near the ice edge, ice morphology information including ice types and their partial concentrations are absent. Nevertheless, the FAL (black dots) presumably marks the separation between discrete floes and a "semi-continuous" ice cover with dispersed leads. The ice condition of a subregion below

90   (before) the FAL was more complex with thinner ice and lower concentration than that above (after) the FAL. Based on the distribution of SAR retrievals, we select the study domain by azimuth from 450 to 750 km and range from 0 to 400 km. Figures 1(b)(c) show the distributions of ice concentration from AMSR2 and ice thickness from SMOS (Soil Moisture and Ocean Salinity, https://icdc.cen.uni-hamburg.de/1/daten/cryo-sphere/l3c-smos-sit.html), respectively, in the region of interest. This work is to retrieve wave attenuation

95   and use the result to calibrate viscoelastic models in thin pack ice (<0.3 m) dominant region.

The Cryosphere
Discussions

Open Access
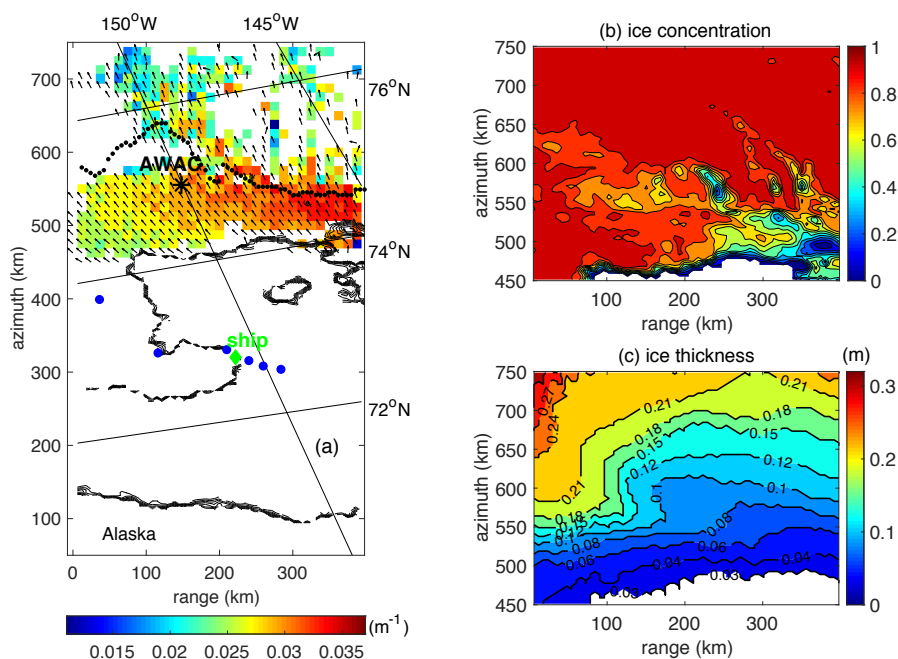
Figure 1. (a) Overview of the retrieved data distribution around 16:50 UTC on 12 October 2015. Colors represent the dominant wavenumber and arrows represent the dominant wave directions. Black dots indicate the first appearance of leads. Locations of the Sikuliaq ship and the relevant buoys are indicated by green diamond and blue dots, respectively. AWAC-I is marked by a black asterisk. Ice edges are indicated by contours of ice concentration < 0.4 from AMSR2 (b)(c) Distributions of ice concentration (AMSR2) and ice thickness (SMOS) in the selected region, respectively.

This paper is organized as follows: site description and wave characteristics are depicted in section 2. We use the directional wave spectra retrieved from the Sentinel-1A SAR imagery to derive the wavenumber-dependent attenuation in section 3. The methodology of model calibration and results are presented in section 4. The methodology of calibrating IC3 used in Cheng et al. (2017) based on wave energy spectrum $E(f, \theta)$ in terms of frequency f needs to be modified for the present wavenumber-based spectra. Section 5 discusses the characteristics of wavelength and attenuation in pack ice, calibrated viscoelastic parameters, and wave attenuation modeling. The final conclusions are given in section 6.

2 Wave characteristics in ice

The retrieved wavenumber-direction spectrum is divided into multiple bins of wavenumber k_r from 0.011 m^{-1} to 0.045 m^{-1} with an increment of 0.002 m^{-1}, and 360 bins in directions with bin width as 1°. The main wave direction θ_{k_r} for each wavenumber k_r is defined as the mean of a Gaussian function fitted to $E(k_r, \theta)$, with an example given in Figure S1 of the supplemental material. Furthermore, we define the dominant wavenumber of the wave spectra, $k_{r,dominant}$, as the one corresponding to the maximum of the directional sum $\int E(k_r, \theta) \, d\theta$.

In Figure 1, $k_{r,dominant}$ generally declines crossing the FAL towards the north. Before the FAL, $k_{r,dominant}$ varies with ice concentration but is insensitive to ice thickness variation and wave directions. After the FAL, $k_{r,dominant}$ decreases in the wave propagating direction associated with the increase of ice thickness, where

120 the ice field is presumably a semi-continuous cover populated with leads.

Figures 2(a)(b) show two-dimensional histograms of the main wave direction for each wavenumber θ_{k_r} before and after the FAL, respectively, where wave direction is defined in the meteorological convention. Grayscale indicates the occurrence frequency of θ_{k_r} in each k_r bin. We observe a significant change of θ_{k_r} crossing the FAL: θ_{k_r} before the FAL spreads from 160° to 190°, while θ_{k_r} is more tightly clustered from

125 180° to 200° after the FAL. The difference before and after the FAL is most significant for $k_r < 0.035$ m^{-1}

For the subsequent spectral analysis, we further restrict k_r to 0.019 m$^{-1} \leq k_r \leq 2\pi/\lambda_c$, where λ_c is the azimuth cutoff indicating the minimum resolvable wavelength from the SAR imagery (Stopa et al., 2015; Ardhuin et al., 2017). Below this wavelength, the patterns of ice-covered ocean surface roughness from SAR imagery are more related to ice features rather than waves (Stopa et al., 2018b). For $k_r < 0.019$ m^{-1}, energy

130 density $E\left(k_r, \theta_{k_r}\right)$ is small with high spatial variation (Figure A1 in the Appendix), hence treated as noise band and removed from further study.
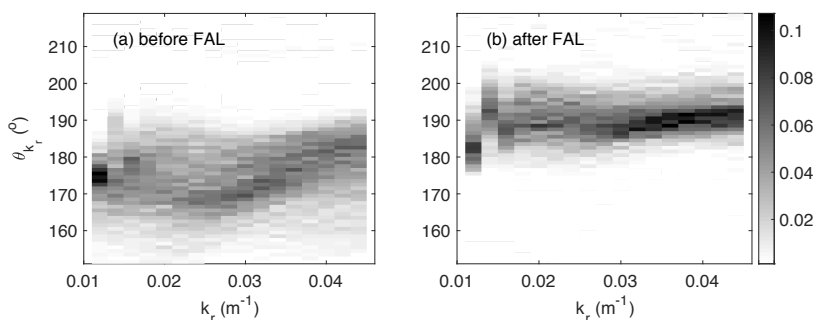
Figure 2. Two-dimensional histogram of θ_{k_r} and k_r collected (a) before and (b) after the FAL. Grayscale represents the occurrence frequency of θ_{k_r} in each k_r bin.

135 The corresponding frequency f (wave period T) range is estimated as 0.067 to 0.11 Hz (9 to 15 s) using the open water dispersion relation, i.e., $(2\pi f)^2 = gk_{ow}$, where g is the gravitational acceleration, k_{ow} indicates the wavenumber in open water. Note the actual range of frequencies in the present case might be different due to the possible change of dispersion relation in pack ice. The dispersion relation cannot be measured from the instantaneous SAR data. Using accelerometers deployed on ice floes (Fox and Haskell, 2001) and from

140 marine radar or buoy data (Collins et al., 2018), it was found that the wavenumber in ice cover region near the open sea (≲10 km) was close to that in open water.

3 Deriving wave attenuation in ice

3.1 Apparent wave attenuation

We define an apparent wave attenuation for each k_r by assuming an exponential decay of the wave spectral

145 densities from location A to location B:

$$\alpha(k_r) = \frac{1}{2D cos(|\bar{\theta} - \theta_{AB}|)} ln\left(\frac{E_A(k_r, \bar{\theta})}{E_B(k_r, \bar{\theta})}\right) \tag{1}$$

where $\bar{\theta} = \frac{\theta_{k_r,A} + \theta_{k_r,B}}{2}$ is the average of the main wave directions at A and B; D and θ_{AB} are the distance and

direction from A to B in the longitude-latitude coordinates, respectively. A selected pair of A and B is named

as a pair hereafter. To reduce the uncertainties of naturally present ice and wave variability, a set of quality

150 control criteria are applied to a pair before further analysis:

1) Ignore substantially oblique waves. Difference between $\bar{\theta}$ and the vector from location A to location B is restricted to $|\bar{\theta} - \theta_{AB}| \leq 15°$.
2) Avoid strong spatial variations of ice condition between A and B. Distance between A and B is restricted to $D \leq 60$ km.

155

3) As the wave state change rapidly across the FAL mentioned in section 2, no pair across the FAL is selected, in order to compare the influence of the ice morphology on wave attenuation.
4) The Pearson correlation coefficient between energy spectra $E_A(k_r, \theta)$ and $E_B(k_r, \theta)$ is greater than 0.9. The similarity of wave spectra patterns indicates that the wave fields from A to B are dominated by the same wave system.

160

5) Exclude outliers of the spectral attenuation where wave energy of B is higher or close to that of A. $\alpha(k_r) > 10^{-6}$ m^{-1} is required.
6) A selected pair has at least 10 data points of $\alpha(k_r)$ to do calibration in section 4.

We obtain 2634 pairs (2194 pairs before the FAL, and 440 pairs after the FAL) through the above criteria to

calculate the apparent wave attenuation $\alpha(k_r)$ by Eq. (1). The empirical thresholds of criteria 2) and 4) are

165 determined based on the sensitivity of the number of selected pairs depending on these values. Figure 3(a)(b)

show two-dimensional histograms of α against k_r before and after the FAL, respectively, where the α

domain is divided into equal 30 bins in log scale from 10^{-6} to 10-4 m^{-1}. Grayscales represent the occurrence

of α at each combined bin of α and k_r. Red curves indicate the most frequent occurrence of $\alpha(k_r)$ against

k_r. It is observed that more data are collected before the FAL, and a slightly increasing trend of $\alpha(k_r)$ versus

170 k_r before the FAL, while $\alpha(k_r)$ obtained after the FAL are mostly lower and independent of k_r.

The range of this apparent spectral attenuation is in agreement with Stopa et al. (2018b), in which, the authors

selected multiple tracks throughout the ice region and focused on the overall decay of the significant wave

height over hundreds of kilometers. The reduction of attenuation crossing the FAL shown in Figure 3 is also

consistent with Stopa et al. (2018b), who reported a drop of attenuation of the significant wave height after

175 the FAL. In the Appendix, we show the results of this long-range attenuation against wavenumber. (Figure

A1). The difference of attenuation obtained by the two methods, one based on short (<60 km) distances to

reduce the effect of ice type variability and the other over long distances (~300 km) is discussed in section

5.
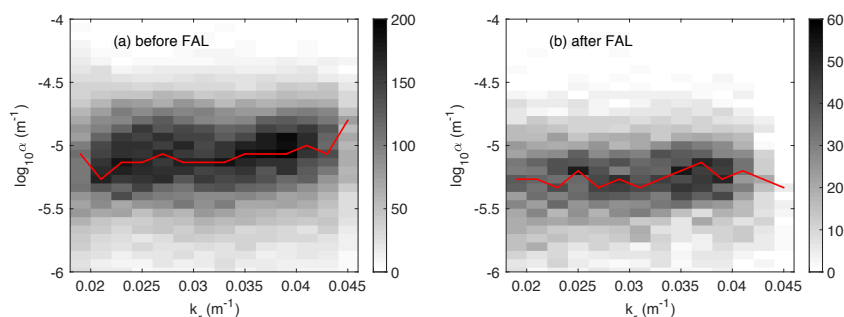
Figure 3. Smoothed two-dimensional histograms of wavenumber k_r and apparent attenuation α, (a) before the FAL and (b) after the FAL. α domain is divided into 30 equal bins in the log scale from 10^{-6} to 10^{-4} m^{-1}. Grayscale indicate the occurrence of α in each α-k_r bin from the selected pairs. The red curve indicates the highest occurrence of α against k_r.

Because of the large study domain and the apparent difference of $k_{r,dominant}$ in the east-west direction before FAL as shown in Figure 1(a), it is worthwhile examining the regional variability. Figure 4 displays the results related to α and k_r in three subdomains from west to east bounded by longitudes: (150ºW, 151ºW), (148ºW, 149ºW) and (146ºW, 147ºW). The left column shows 467, 233 and 132 pairs selected in the three longitude bins, respectively. Each segment indicates a pair selected in section 3.1, with ends correspond to the locations A, B and its color indicates the mean ice thickness between the two. In the middle column, the α values corresponding to $k_r = 0.019, 0.025, 0.031$ and 0.039 m^{-1} obtained from these pairs are separated into two groups: before and after the FAL. In each subdomain delineated by the longitude and the FAL, the distribution of α for each k_r is presented by a violin plot, whose width indicates the probability density distribution of α and a circle marker inside indicates the median. These violin plots show that α before the FAL is larger than that after the FAL for all k_r in all three subdomains. We note that the sample size after the FAL in the easternmost subdomain (146ºW, 147ºW) is the lowest, corresponding to the largest variability of the violin plots. In the right column, the power spectral densities (PSDs) retrieved at locations of the ends of the selected pairs in the left column are given. Curves indicate the averaged PSD per 0.1 degree in latitudes, with latitude marked by colors. As defined earlier, k_r associated with the peak of a PSD curve is $k_{r,dominant}$. Before the FAL the magnitude of PSD drops rapidly while $k_{r,dominant}$ varies slightly as the increase of latitude. In contrast, the PSDs vary slowly after the FAL while $k_{r,dominant}$ decreases quickly. Note at high latitudes, PSD at $k_{r,dominant}$(red) is higher than that of the same wavenumber at low latitudes. We will revisit this phenomenon in the discussion section.
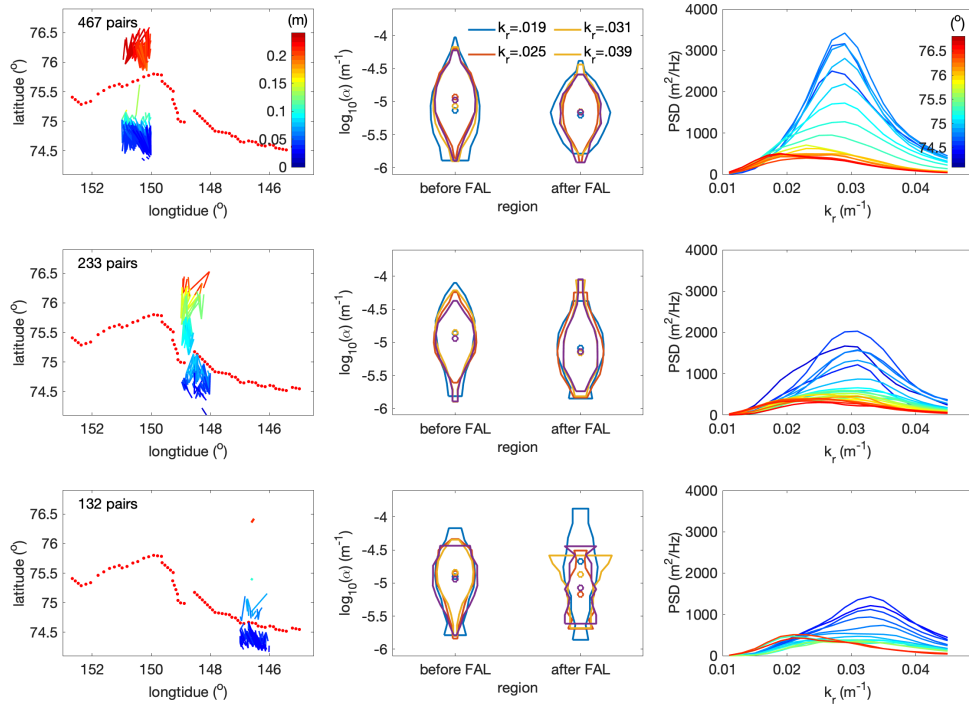
Figure 4. Close view in three selected longitude intervals: (150ºW, 151ºW), (148ºW, 149ºW) and (146ºW, 147ºW). (Left column) Geological distribution of the selected pairs, each of which is represented by a segment with color indicating the mean ice thickness. Red dots represent the FAL. (Middle column) Violin plots of the relevant α grouped by wavenumbers and before/after the FAL. (Right column) Evolution of PSD of SAR retrieved wave spectra per 0.1º in latitude in the subdomain. Note in the rightmost interval (bottom row) the red PSD curves correspond to the few very short red segments near 76.5ºN.

3.2 Wave attenuation due to ice effect

Following Eq. (1), the apparent attenuation obtained above is determined by the energy difference between two locations. This apparent attenuation is the result of multiple source terms, including the wind input S_{in}, the dissipation through wave breaking S_{ds}, the energy transfer due to nonlinear interactions among spectral components S_{nl}, and the dissipation/scattering of wave energy due to ice cover S_{ice}. The radiative transfer equation for surface waves concerning all the above effects is

$$\frac{\partial E}{\partial t} + \frac{\partial (c_g + U)E}{\partial x} = (1 - C)(S_{in} + S_{ds}) + S_{nl} + CS_{ice} \tag{2}$$

where $E = E(k_r, \theta, x)$ is the power spectral density depending on wavenumber, direction and location x; c_g is the group velocity; U is the current velocity. Note that U in this region is below 0.1 m/s, according to OSCAR (Ocean Surface Current Analyses Real-time, https://www.esr.org/research/oscar/). Because the current speed is at least one order of magnitude below the estimated c_g using the open water dispersion relation, we may drop it from Eq. (2). Furthermore, by assuming c_g to be relatively constant along x and

8

adopting the exponential wave decay (i.e., $E(k_r, \theta, x) = E(k_r, \theta, x = 0)e^{-2\alpha x}$), we have $\frac{\partial(c_g + U)E}{\partial x} \approx c_g \frac{\partial E}{\partial x} = -2c_g \alpha E$.

Next, we examine the temporal derivative of wave energy $\frac{\partial E}{\partial t}$. It is challenging to calculate $\frac{\partial E}{\partial t}$ from the nearly

225   instantaneous SAR imagery. Instead, we estimate $\frac{\partial E}{\partial t}$ using hourly wave spectra data from two sources around the time stamp of the SAR imagery: the in-situ AWAC-I marked in Figure 1 and the WW3 simulations of the whole domain (REF run of Ardhuin et al., 2018). From the AWAC-I data, we obtain $\frac{\partial E}{\partial t}$ and compare that with $c_g \frac{\partial E}{\partial x}$ using SAR retrieved wave data at the AWAC-I site. From the WW3 simulations, we obtain both terms over the whole study domain. Both results consistently show that $\frac{\partial E}{\partial t}$ is at least two orders of magnitude

230   below $c_g \frac{\partial E}{\partial x}$. Thus, $\frac{\partial E}{\partial t}$ is dropped from Eq. (2).

The other source terms S_{in} and S_{ds} are estimated using formulations from Snyder et al. (1981) and Komen et al. (1984). For S_{nl}, we select the Discrete Interaction Approximation (DIA, Hasselmann et al., 1985a, b) to estimate its value. These formulations and associated coefficients are described in Cheng et al. (2017). Wherever needed in these formulations, f is approximated by the open water dispersion relation with the

235   measured k_r (Collins et al., 2018). Ice concentration is from AMSR2, ice thickness is from SMOS, and wind data is from the Climate Forecast System Reanalysis (CFSR, Saha et al., 2010).

Ice-induced wave attenuation is known from dissipation of wave energy and scattering of waves (e.g., Wadhams et al., 1988; Squire et al., 1995; Montiel et al., 2018). Here we attribute the attenuation entirely to the dissipative process with the following arguments. Ardhuin et al. (2018) reported that in the studied region,

240   ice floe scattering is a weaker effect on wave attenuation compared with other processes, including the boundary layer beneath ice, inelastic flexing of ice cover, and wave-induced ice fracture. The inelastic flexing and ice fracture may be considered as part of the dissipative mechanism within the ice cover already included in the viscous coefficient, but scattering is a re-distribution of energy, which must be isolated from the apparent attenuation before using the data to calibrate the viscoelastic models. We estimate the scattering

245   effect based on the study of Bennetts and Squire (2012) as follows. In that study, wave attenuation by floes, cracks and pressure ridges were examined. In the absence of in-situ observations, we assume that few and small ridges are present in the studied ice cover (< 25 cm), hence the effect of ridges is negligible. In our case of long waves propagating through such thin ice cover, Bennetts and Squire (2012) have shown that the floes produce much more attenuation than the cracks. Without in-situ observation, WW3 simulations (REF run in

250   Ardhuin et al., 2018) implementing wave-induced fracturing of ice floes gives a range of estimated maximum floe diameter from 70 to 150 m. Using this range of floe diameter, the theoretical scattering results from Bennetts and Squire (2012) indicate that the floe scattering-induced attenuation is about 10^{-7} m^{-1}, which is negligible compared to the α shown in Figure 3.

With all the above simplifications and the assumed exponential decay of wave energy, Eq. (2) becomes:

255
$$-c_g 2\alpha E = (1 - C)(S_{in} + S_{ds}) + S_{nl} - C2c_g k_i^m E \tag{3}$$

which yields

$$k_i^m = \frac{2c_g\alpha E + (1-C)(S_{in}+S_{ds}) + S_{nl}}{2Cc_g E} \tag{4}$$

where k_i^m is the attenuation rate due to the ice cover. Figure 5 shows two-dimensional histograms of α against k_r before and after the FAL, as in Figure 3. Not surprisingly, since wind effect is low due to the low open water fraction in the study region, and the relatively short distances between the pairs for the nonlinear transfer of energy to accumulate, we observe that k_i^m is very close to the apparent attenuation α, and will be further discussed in the discussion section.
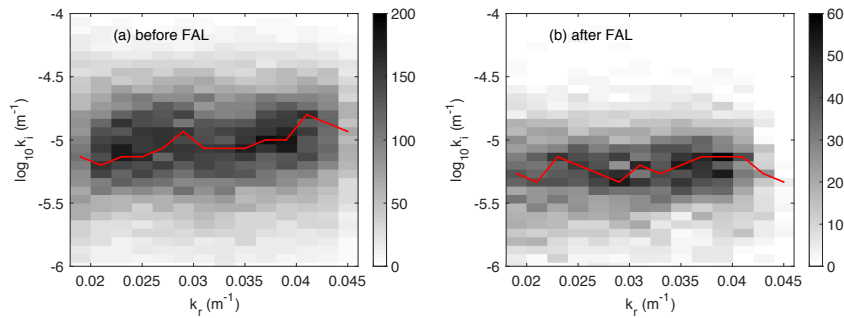

Figure 5. Similar as Figure 3, two-dimensional histogram of k_i^m against k_r.

4 Wave-in-ice model calibration

In this section, we present the calibration of the WS model and the FS model. In both models, k_r, k_i are solved from the respective dispersion relations for given ice thickness and viscoelastic properties. An optimization procedure is introduced to select the viscoelastic parameters that minimize the difference between the model k_i and the k_i^m obtained from the SAR over the entire range of k_r.

4.1 Dispersion relation

The dispersion relations of the two models are written as

$$\sigma^2 - Qgk\tanh kH = 0 \tag{5a}$$

For the WS model,

$$Q = 1 + \frac{\rho_{ice}}{\rho_{water}} \frac{(g^2k^2 - N^4 - 16k^6\alpha^2 v_e^4)S_kS_\alpha - 8k^3\alpha v_e^2 N^2(C_kC_\alpha - 1)}{gk(4k^3\alpha v_e^2 S_kC_\alpha + N^2 S_\alpha C_k - gkS_kS_\alpha)} \tag{5b}$$

For the FS model,

$$Q = \frac{G_v h^3}{6\rho_{water}g}(1+V)k^4 - \frac{\rho_{ice}h\sigma^2}{\rho_{water}g} + 1 \tag{5c}$$

where H is water depth, $\sigma = 2\pi f$ is the angular frequency, ρ_{ice} and ρ_{water} are the densities of ice and water, respectively, $k = k_r + ik_i$ is a complex wavenumber, $S_k = \sinh kh$, $S_\alpha = \sinh \alpha h$, $C_k = \cosh kh$, $C_\alpha = \cosh \alpha h$, h is the ice thickness, $\alpha^2 = k^2 - \frac{i\sigma}{v_e}$, $N = \sigma + 2ik^2 v_e$, $G_v = G - i\sigma v\rho_{ice}$ and $v_e = v + \frac{iG}{\rho_{ice}\sigma}$, V is the Poisson's ratio. Equivalent shear modulus G and kinematic viscosity v in both models are to be calibrated.

The Cryosphere
Discussions
Open Access

In this study, we use $H = 1000$ m for deep water, $\rho_{water} = 1025$ kg/m^3, $\rho_{ice} = 922.5$ kg/m^3 and $V = 0.3$ for ice.

4.2 Calibration methodology

For each pair selected in section 3, we optimize G, ν by fitting modeled k_i to the measured k_i^m over the k_r^m

285   domain. Note that k_i, k_r in the models are solved simultaneously for an array of f. We need to convert the theoretical k_i-f relation to k_i-k_r^m. Specifically, for given G and ν, we solve arrays of k_r and k_i through Eq. (5) for f from 0.0001 Hz to 1 Hz, and then interpolate the results to obtain the theoretical k_i at each k_r^m. The objective function for the optimization is defined as the weighted sum of the differences between k_i and k_i^m over k_r^m, i.e.,

290
$$F = \min_{G,\nu} \| w(k_r^m)(k_i^m - k_i) \|_2 \qquad (6)$$

where $w(k_r^m)$ is a weighting factor to account for the distributions of wave energy and attenuation rate. Cheng et al. (2017) tested using $w = \int E(\theta, f) d\theta$ and $\int E(\theta, f) f^4 d\theta$ in calibrating the WS model. In that study, the measured data had a range of f varied from 0.05 to 0.5 Hz, and attenuation rate varied from 10^{-6} to 10^{-3} m^2/s. The authors found using $w = \int E(\theta, f) d\theta$ fitted attenuation at the most energetic wave

295   component, while $w = \int E(\theta, f) f^4 d\theta$ performed better to capture significant increasing of k_i at high frequencies. No weighting factor could produce a fitting over the entire spectral attenuation curve. For the present study, the variation of spectral attenuation is small as shown in Figure 5 with no particular region of emphasis, we choose $w = \sqrt{\int E(\theta, k_r) d\theta}$ which has a broad band around the peak energy of the wave field. We choose a search domain (10^{-7} Pa $\leq G \leq 10^{10}$ Pa and 10^{-4} m^2/s $\leq \nu \leq 10^4$ m^2/s) for the WS model. This

300   search domain covers all other reported viscoelastic values for ice covers (e.g., Newyear and Martin, 1999; Doble et al., 2015; Zhao and Shen, 2015; Rabault et al., 2017). For the FS model, it is known that very large G, ν are needed to obtain the level of k_i observed (Mosig et al., 2015). We thus choose a large search domain 10 Pa $\leq G \leq 10^{20}$ Pa and $10 \leq \nu \leq 10^{15}$ m^2/s. This parameter range is far beyond the measured data from solid ice (Weeks and Assur, 1967). The global optimization procedure is performed by the genetic algorithm

305   using function *ga* in MATLAB and Global Optimization Algorithm Toolbox (R2016a).

4.3 Results

For the WS model, the optimized G, ν are gathered into a small cluster around $G \cong 10^{-4}$ Pa and a large cluster around $G \cong 10^5$ Pa with large variation in ν. The existence of two separate clusters of calibrated results was also found in grease/pancake mixtures near the ice edge (Cheng et al., 2017). As multiple solutions

310   could be obtained in solving optimal problem of the nonlinear system Eq. (5), constraints are applied to select solutions that are physical. In the optimization, we reject the solutions around $G = 10^{-4}$ Pa, and solutions with ν near 10^4 m^2/s that the residual from Eq. (6) is insensitive to G. Because both situations imply that the model becomes viscous dominant, inconsistent with the physical behaviors of the pack ice. Scatter plots of the remaining data points (G, ν) are presented by Figure S2 in the supplemental material. Furthermore, we

315 apply the bivariate Gaussian distribution to the rest of points to obtain the 90% probability range of (G, v) before and after the FAL, respectively. Means and covariances of the related probability density functions are given in Table 1. Slight difference of distributions of G, v before and after the FAL is noticed. The mean of elasticity (viscosity) is slight lower (higher) before the FAL than that after the FAL. The results imply that the ice layer behaves more elastic in the inner ice field and more viscous towards the ice edge. It is worth

320 noting that the ranges of both G and v are about one order of magnitude greater than those of the grease/pancake ice (Cheng et al., 2017). As expected, the effective elasticity in the WS model for more solid ice is closer to the elastic modulus of sea ice.

Table 1. The mean (μ) and covariance (cov) of $X = \log_{10} G$ and $Y = \log_{10} v$.

|	μ_X	μ_Y	$cov(X,X)$	$cov(X,Y)$	$cov(Y,Y)$
WS Model					
Before FAL	5.07	1.51	0.07	0.07	0.81
After FAL	5.25	1.32	0.11	0.27	1.26
FS Model					
Before FAL	17.39	10.82	2.83	1.42	1.00
After FAL	16.26	9.51	1.90	0.95	0.75

For the FS model, the calibrated (G, v) are clustered, where scatter plots of (G, v) are given in Figure S3 in

325 the supplemental material. Hence all data points are used in the bivariate Gaussian fitting. The resulting mean and covariance values are also given in Table 1. Scatter plots of (G, v) are given in Figure S3 in the supplemental material. Notice that the mean values of G, v from the FS model are extremely larger than the intrinsic values of ice. The distribution of calibrated values is further discussed in the discussion section. Hereafter we only elaborate on results of the WS model. Figures 6(a) shows the overall comparison of k_i-k_r

330 between the measurements (Gray) and the WS model (black). Both the median (solid curve) and 90% boundaries (dash curves) are in good agreement. In Figure 6(a), we superimpose an empirical model from Meylan et al. (2014), which is also included in WW3 to account for the ice effect as switch IC4. By fitting the wave buoy data from the Antarctic MIZ obtained in 2012, Meylan et al. (2014) proposed a simple period-dependent attenuation rate $k_i(T) = \frac{2.12 \times 10^{-3}}{T^2} + \frac{4.59 \times 10^{-2}}{T^4}$, which is converted into a k_i-k_r relation through the

335 open water dispersion relation. The empirical formula predicted that attenuation was consistent with the range we obtained here, but with a higher sensitivity to k_r. Figure 6(b) shows the normalized wavenumber $\frac{k_r}{k_{ow}}$ against f using the optimized G, v in the WS model. The deviation of $\frac{k_r}{k_{ow}}$ from 1 is less than 5%. The counterpart of the FS model is given Figure S4 in the supplemental material.
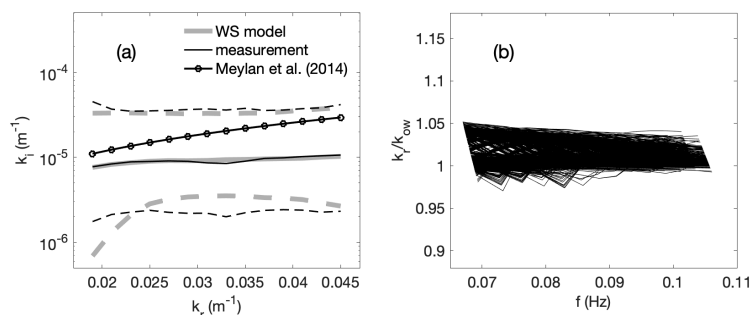
Figure 6. (a) Comparison of ice-induced attenuation k_i between measured data and the WS model results; Solid lines are mean values and dashed lines are 90% confidence intervals. Gray-thick lines are the calibrated WS model and black thin lines from the data. Black line with symbol is the empirical model from Meylan et al. (2014); (b) the corresponding k_r/k_{ow} from the calibrated WS model against wave frequency.

Figures 7(a)(b) show distributions of calibrated G and ν from the WS model in the azimuth-range domain, respectively. Contours represent ice thickness distribution from SMOS. The FAL is marked as red dots. The spatial domain is divided into 12.5 km × 12.5 km cells to enhance visualization. Cell color indicates the averaged value of $\log_{10}G$ and $\log_{10}\nu$ of all pairs with midpoints inside the cell. Ignoring the outliers, it shows that G is generally larger after the FAL (thicker ice with leads) than before the FAL, while ν has an opposite trend. Note that the outliers could be from multiple sources, such as noise in the retrieved wave data, spatial variability of ice condition, as well as assumptions made in selecting pairs and calculating attenuation. The counterpart of the FS model is given in Figure S5 in the supplemental material.
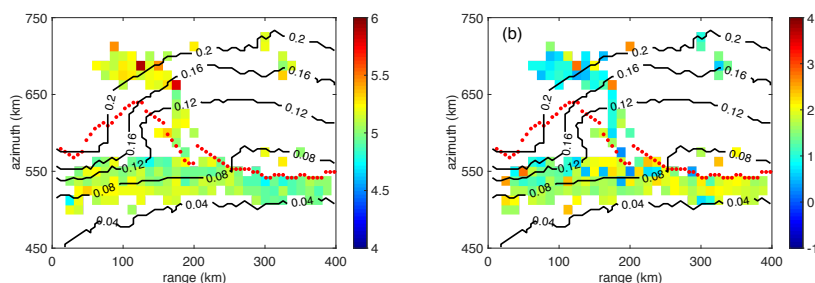
Figure 7. (a) Distribution of $\log_{10}G$ in averaged 12.5 km×12.5 km grid in the range-azimuth plane. Cell color indicates the averaged $\log_{10}G$ of all pairs with midpoints inside a cell; Contours indicate SMOS ice thickness; Red dots indicate the FAL (b) Same as panel (a) except replacing $\log_{10}G$ with $\log_{10}\nu$.

5 Discussion

In this section we discuss some key wave characteristics mentioned in the analysis, and the behaviors of calibrated model parameters. Some thoughts about wave-in-ice modelling are provided at the end.

5.1 Evolution of wave characteristics

360   The behaviors of $k_{r,dominant}$ and PSD in Figures 1 and 4 may come from multiple mechanisms. The decrease of $k_{r,dominant}$ towards the interior ice is in agreement with a similar study in the MIZ (Shen et al., 2018), as well as the lengthening of dominant wave periods commonly reported in many field observations (e.g., Robin, 1963; Wadhams et al., 1988; Marko, 2003; Kohout et al. 2014; Collins et al., 2015). The phenomenon is commonly explained by the low pass filter mechanism in literature. That is, higher frequency waves are

365   preferentially attenuated, thus the power spectrum peak shifts to longer waves. However, though this mechanism is supported by the increasing trend of k_i with increasing wavenumber before the FAL, it is insufficient to explain the observations after the FAL, where the k_i-k_r curve is practically flat (Figure 5) and the peak of PSD shifts toward lower k_r as latitude increases (Figure 4). Two other mechanisms also may cause a downshift of the wave energy towards lower wave numbers. One is the change of dispersion relation,

370   so that the wavelength grows deeper into the ice cover. The other is the nonlinear transfer between wave components which move the energy in the main wave frequency into the low frequency components. How to quantify these mechanisms is still an open question with little data especially in pack ice, where the skills in observations are still developing. A critical information is the wave period in wave spectra, especially in the region after the FAL.

375   The attenuation rate obtained in this study (~10^{-5} m^2/s) against wavenumber shows a slight increasing trend before the FAL, while nearly flat trend and lower after the FAL. Similar magnitude of attenuation is found in the MIZ in both Arctic and Antarctic as reported in previous studies in the same period range but larger for shorter periods (e.g., Meylan et al., 2014; Doble et al., 2015; Rogers et al., 2016; Cheng et al., 2017). The analysis of attenuation against wavenumber in section 3 is obtained for pairs of observations over relatively

380   short distances (<60 km). In the Appendix, we present another method to determine the overall attenuation, similar to the analysis of the attenuation of the significant wave height shown in Stopa et al. (2018b). By analyzing wavenumber by wavenumber over the entire space where the SAR data covers, the apparent attenuation coefficient is obtained by fitting hundreds of data over long distance, ignoring the higher variation of ice thickness (0.01~0.3m) and the shift of dominant wavenumber from the PSD curves. The results are

385   shown in Figure A2. In some cases, we can even have negative values of this attenuation, meaning energy increases as wave propagates. What we would like to emphasize by showing this result is that over a very long-distance ice condition can change significantly, in addition to nonlinear energy transfer and wind input/dissipation, thus long-distance spectral analysis may become meaningless.

5.2 model calibration

390   The covariance values of the calibrated viscoelastic parameters are greater than those found in grease/pancake ice using buoy data (Cheng et al. 2017). In processing the SAR data, there are many challenges to be dealt with. It is extremely difficult to separate 1) sea ice variability, 2) wave height variability, and 3) instrument variability (speckle and in-coherent SAR noise). All of these influence the variations we see in the wave spectral data. The mask used in determining qualified data used in this study was described in Stopa et al.

395　(2018b). Still, the scatter of the spectral attenuation shown in Figure 3 is significant even after the filtering described in section 3.1. This data scatter results in a large range of calibrated model parameters. We believe that the scatter of calibrated G, v in both WS and FS models could be narrowed down by reducing the uncertainty of measured attenuation data. We also believe that for the FS model the calibrated values and spread could be reduced by modifying the objective function with additional constraint on the wavenumber,

400　which presently shows an extremely large range as shown in Figure S4. Regardless, the FS model needs much larger G, v to produce attenuation rates comparable to the observed data. This is the case not only for the pack ice but also for the MIZ. When analyzing data from the Antarctic MIZ reported in Kohout and Williams (2013), and by further constraining $k_r = k_{ow}/1.7$, Mosig et al. (2015) obtained $G = 4.9 \times 10^{12} \, \text{Pa}, v = 5 \times 10^7 \, \text{m}^2/\text{s}$. Though far below the present case, these values are still orders of magnitude

405　above the intrinsic values measured from solid ice (Weeks and Assure, 1967). Meylan et al. (2018) discussed the attenuation behavior among different dissipative models by assuming small $|k_r - k_{ow}|$. Specifically, they showed that the FS model produced $k_i \approx \frac{\rho_{ice}(1+V)h^3}{6\rho_{water}g^6} v\sigma^{11}$ and the pure viscous case of WS model (i.e., Keller (1998)'s model) produced $k_i \approx \frac{4\rho_{ice}h}{\rho_{water}g^4} v\sigma^7$. The higher the power in σ, the higher v is to match the measured k_i in the high period (low frequency) waves range. The FS model also naturally leads to large G.

410　As shown in Mosig et al. (2015), inverting the dispersion relation shown in Eqs. (5a,c) gives $G - i\sigma\rho_i v = 6\frac{\rho_w\sigma^2 - gk\rho_w - hk\rho_i\sigma^2}{h^3k^5(1+V)}$. The leading term of which in small k_r yields $G \approx O(k_r^{-5})$.

5.3 Thoughts of modelling wave-ice interaction

Damping models play a crucial role in spectral attenuation. At present, to use any specific model to describe wave attenuation is tentative. Identified damping mechanisms are many. For instance, boundary layer under

415　the ice cover (Liu and Mollo-Christensen, 1988; Smith and Thomson, 2019), spilling of water over the ice cover and interactions between floes (Bennetts and Williams, 2015), jet formation between colliding floes (Rabault, 2019), have all been reported in laboratory or field studies. A full waves-in-ice model that clarifies all important mechanisms is not yet available. While theoretical improvements are needed to better model wave propagation through various types of ice covers, practical applications cannot wait. Calibrated models

420　that are capable of reproducing key observations must be developed in parallel to model improvements. The present study provides a viable way to calibrate two such models available in WW3. These models lump all dissipative mechanisms in the ice cover into a viscous term. This type of model calibration studies has two obvious utilities. One, with proper calibration, models can capture the attenuation of the most energetic part of the wave spectrum. Two, the discrepancies may be used to motivate model development that includes

425　missing mechanisms, thereby help future model development. Because different physical processes may play different roles under different ice morphology, collecting wave data to calibrate these models under various ice types is necessary. Finally, more observations with higher quality data will improve modeling of the wave-ice interaction and the robustness of the models.

6 Conclusions

430　The wave spectra were retrieved from SAR imagery in the young pack ice predominant area in Beaufort Sea in 12 October 2015, further north of the grease/pancake ice region along the ship and buoy tracks. According to the analysis of data retrieved over several hundred kilometers, the observed decrease of wave energy and lengthening of dominant waves towards the interior ice are consistent with earlier in-situ observations. We investigate wave attenuation of dominant spectral densities per wavenumber between two arbitrary locations

435　in the region. Similar attenuation rates are observed for all wavenumbers from 0.019 to 0.045 m^{-1} (estimated wave period from 9 to 15 s). We then use the wave attenuation rates to calibrate two viscoelastic-type wave-in-ice models. Both models can generally match the observed attenuation corresponding to the energetic portion of the wave spectra, with large difference on dispersion. For the WS model, the calibrated shear modulus (viscous parameter) in the region beyond the first appearance of leads with thicker ice is slightly

440　larger (smaller) than that of the region closer to ice edge before the first appearance of leads. The resulting wavenumber is within 5% of that produced from the open water dispersion.

Wave-ice interaction is complicated due to many co-existing physical processes. At present no models have fully integrated all identified processes. However, marine operations in the ice-covered seas need wave forecasts. The present study demonstrates a method based on measured data to calibrate existing models, so

445　that they can be applied to meet the operational needs. As the models improve, further calibration exercises may be performed accordingly. For example, the eddy viscosity model (Liu and Mollo-Christensen, 1988) attributed the wave attenuation entirely to the water body under the ice cover. This model is also included in WW3, with the eddy viscosity as a tuning parameter. The present analysis can also be used to calibrate that model. From a physical point of view, dissipative mechanisms may be present simultaneously inside the ice

450　cover and the water body underneath. However, calibration of complex models with multiple co-existing processes is a difficult task which requires much more dedicated study.

We conclude by noting that high resolution spatial data from remote sensing provide new opportunities to investigate the wave-ice interaction over a large distance and different ice types. However, details of ice types and temporal observations are in development. To reach a full understanding and thus a complete waves-in-

455　ice model requires collaboration from observation and modeling efforts.

Appendix

We investigate the decay of the dominant energy component $E(k_r, \theta_{k_r})$ over a long distance along selected tracks with fixed longitude (145ºW, 146ºW, …, 150ºW). Figure A1 shows $E(k_r, \theta_{k_r})$ (blue dots) collected within a given longitude interval 150 ± 0.1ºW starting from 74.5ºN towards the north. $E(k_r)$ for $k_r < 0.019$

460　m^{-1} is too scattered to show any attenuation trend. While as k_r increases, the data become tighter with a clear decay trend. To obtain attenuation coefficient $\hat{\alpha}(k_r)$, we fit the $E(k_r, \theta_{k_r})$ by an exponential curve (black line) in each panel based on an exponential wave decay assumption.

16
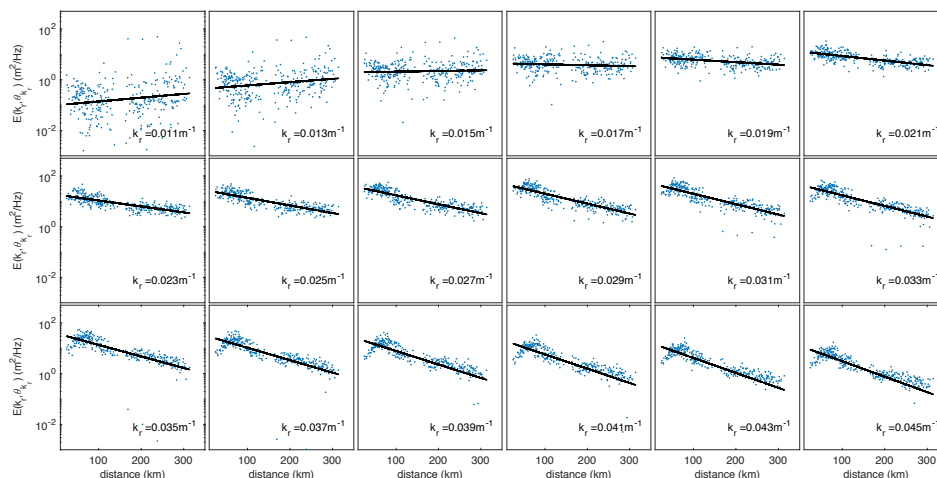
Figure A1. Evolution of dominant wave energy component over long distance at different wavenumbers. The horizontal axis is the distance along a longitude from 74.5ºN towards the north.

The resulting $\hat{\alpha}(k_r)$ against k_r is shown in Figure A2, as well as another five curves associated with different longitudes, processed in the same way. Figure A2 shows an increasing trend of $\hat{\alpha}(k_r)$ against k_r as expected, and $\hat{\alpha}(k_r < 0.019 \text{ m}^{-1})$ are mostly negative. While this plain method blinds the variation of ice morphology and peak shifting of the power spectra density, thus it is insufficient to understand the damping mechanism in water-ice interaction. Hence, as our interest is to determine the attenuation in more consistent ice conditions, shorter distance between measuring points is adopted in the main body.
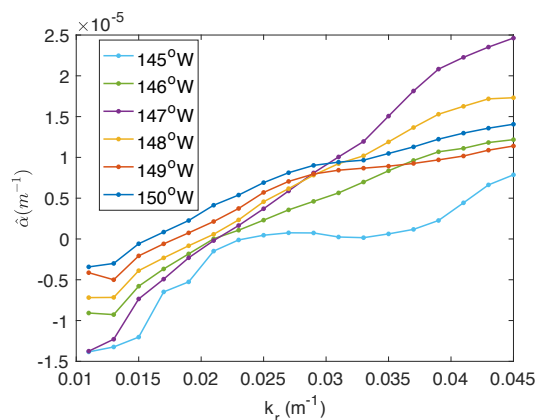
Figure A2. $\hat{\alpha}$ against k_r of different longitude tracks.

Code and data availability

The code and data necessary to reproduce the results presented in this paper can be obtained from the corresponding author.

The Cryosphere

Discussions

Open Access

EGU

Author contribution

Stopa and Ardhuin retrieved the wave spectra dataset from SAR images. Cheng and Shen planned the research and prepared the manuscript with contributions from all authors. Cheng performed the analysis.

480 **Competing interests**

The authors declare that they have no conflict of interest.

References

Ardhuin, F., Stopa, J., Chapron, B., Collard, F., Smith, M., Thomson, J., Doble, M., Blomquist, B., Persson, O., Collins III, C. O. and Wadhams P.: Measuring ocean waves in sea ice using SAR imagery: A quasi-deterministic approach evaluated with Sentinel-1 and in situ data, Remote sensing of Environment, 189, 211-
495 222, 2017.

Ardhuin, F., Boutin, G., Stopa, J., Girard-Ardhuin, F., Melsheimer, C., Thomson, J., Kohout, A., Doble, M., and Wadhams, P.: Wave attenuation through an Arctic marginal ice zone on 12 October 2015: 2. Numerical modeling of waves and associated ice breakup, Journal of Geophysical Research: Oceans, 123, 5652-5668, 2018.

500 Bennetts, L. G., and Squire, V. A.: Model sensitivity analysis of scattering-induced attenuation of ice-coupled waves, Ocean Modelling, 45, 1-13, 2012.

Bennetts, L. G., and Williams, T. D.: Water wave transmission by an array of floating discs, Proceedings of the Royal Society A: Mathematical, Physical and Engineering Sciences, 471, 20140698, 2015.

Cheng, S., Rogers, W. E., Thomson, J., Smith, M., Doble, M. J., Wadhams, P., Kohout, A. L., Lund, B.,
505 Persson, O. P., Collins III, C. O., Ackley, C. F., Montiel F., and Shen H. H.: Calibrating a viscoelastic sea ice

model for wave propagation in the Arctic fall marginal ice zone, Journal of Geophysical Research: Oceans, 122, 8770-8793, 2017.

Collins III, C. O., Rogers, W. E., Marchenko, A., and Babanin, A. V.: In situ measurements of an energetic wave event in the Arctic marginal ice zone, Geophysical Research Letters, 42, 1863-1870, 2015.

510   Collins III, C. O., Doble, M., Lund, B., and Smith, M.: Observations of surface wave dispersion in the marginal ice zone, Journal of Geophysical Research: Oceans, 123, 3336-3354, 2018.

Comiso, J. C., Parkinson, C. L., Gersten, R., and Stock, L.: Accelerated decline in the Arctic sea ice cover, Geophysical research letters, 35, 2008.

De Carolis, G., Olla, P., and Pignagnoli, L.: Effective viscosity of grease ice in linearized gravity waves, 515   Journal of Fluid Mechanics, 535, 369-381, 2005.

Doble, M. J., De Carolis, G., Meylan, M. H., Bidlot, J. R., and Wadhams, P.: Relating wave attenuation to pancake ice thickness, using field measurements and model results, Geophysical Research Letters, 42, 4473-4481, 2015.

Fox, C., and Haskell, T. G.: Ocean wave speed in the Antarctic marginal ice zone, Annals of Glaciology, 33, 520   350-354, 2001.

Hasselmann, S., and Hasselmann, K.: Computations and parameterizations of the nonlinear energy transfer in a gravity-wave spectrum. Part I: A new method for efficient computations of the exact nonlinear transfer integral, Journal of Physical Oceanography, 15, 1369-1377, 1985.

Hasselmann, S., Hasselmann, K., Allender, J. H., and Barnett, T. P.: Computations and parameterizations of 525   the nonlinear energy transfer in a gravity-wave specturm. Part II: Parameterizations of the nonlinear energy transfer for application in wave models, Journal of Physical Oceanography, 15, 1378-1391, 1985.

Keller, J. B.: Gravity waves on ice-covered water, Journal of Geophysical Research: Oceans, 103, 7663-7669, 1998.

Kohout, A. L., Williams, M. J. M., Dean, S. M., and Meylan, M. H.: Storm-induced sea-ice breakup and the 530   implications for ice extent, Nature, 509, 604-607, 10.1038/nature13262, 2014.

Kohout, A. L., Williams, M. J. M., Toyota, T., Lieser, J., and Hutchings, J.: In situ observations of wave-induced sea ice breakup, Deep Sea Research Part II: Topical Studies in Oceanography, 131, 22-27, 2016.

Komen, G., Hasselmann, K., and Hasselmann, K.: On the existence of a fully developed wind-sea spectrum, Journal of physical oceanography, 14, 1271-1285, 1984.

535   Lange, M., Ackley, S., Wadhams, P., Dieckmann, G., and Eicken, H.: Development of sea ice in the Weddell Sea, Annals of Glaciology, 12, 92-96, 1989.

Liu, A. K., and Mollo-Christensen, E.: Wave propagation in a solid ice pack, Journal of Physical Oceanography, 18, 1702-1712, 1988.

Marko, J. R.: Observations and analyses of an intense waves-in-ice event in the Sea of Okhotsk, Journal of 540   Geophysical Research: Oceans, 108, 2003.

MATLAB and Global Optimization Toolbox R2016a: The MathWorks Inc., Natick, Massachusetts, United States, 2016.

Meylan, M. H., Bennetts, L. G., and Kohout, A. L.: In situ measurements and analysis of ocean waves in the Antarctic marginal ice zone, Geophysical Research Letters, 41, 5046-5051, 2014.

545 Meylan, M. H., Bennetts, L. G., Mosig, J. E., Rogers, W. E., Doble, M. J., and Peter, M. A.: Dispersion relations, power laws, and energy loss for waves in the marginal ice zone, Journal of Geophysical Research: Oceans, 123, 3322-3335, 2018.

Montiel, F., Squire, V. A., Doble, M., Thomson, J., and Wadhams, P.: Attenuation and directional spreading of ocean waves during a storm event in the autumn Beaufort Sea marginal ice zone, Journal of Geophysical

550 Research: Oceans, 123, 5912-5932, 2018.

Mosig, J. E., Montiel, F., and Squire, V. A.: Comparison of viscoelastic-type models for ocean wave attenuation in ice-covered seas, Journal of Geophysical Research: Oceans, 120, 6072-6090, 2015.

Newyear, K., and Martin, S.: Comparison of laboratory data with a viscous two-layer model of wave propagation in grease ice, Journal of Geophysical Research: Oceans, 104, 7837-7840, 1999.

555 Rabault, J., Sutherland, G., Gundersen, O., and Jensen, A.: Measurements of wave damping by a grease ice slick in Svalbard using off-the-shelf sensors and open-source electronics, Journal of Glaciology, 63, 372-381, 2017.

Rabault, J., Sutherland, G., Jensen, A., Christensen, K. H., and Marchenko, A.: Experiments on wave propagation in grease ice: combined wave gauges and particle image velocimetry measurements, Journal of

560 Fluid Mechanics, 864, 876-898, 2019.

Robin, G. d. Q.: Wave propagation through fields of pack ice, Philosophical Transactions of the Royal Society of London. Series A, Mathematical and Physical Sciences, 255, 313-339, 1963.

Rogers, W. E., Thomson, J., Shen, H. H., Doble, M. J., Wadhams, P., and Cheng, S.: Dissipation of wind waves by pancake and frazil ice in the autumn B eaufort S ea, Journal of Geophysical Research: Oceans, 121,

565 7991-8007, 2016.

Saha, S., Moorthi, S., Pan, H. L., Wu, X., Wang, J., Nadiga, S., Tripp, P., Kistler, R., Woollen, J., and Behringer, D.: The NCEP climate forecast system reanalysis, Bulletin of the American Meteorological Society, 91, 1015-1058, 2010.

Shen, H., Perrie, W., Hu, Y., and He, Y.: Remote sensing of waves propagating in the marginal ice zone by

570 SAR, Journal of Geophysical Research: Oceans, 123, 189-200, 2018.

Shen, H. H., Ackley, S. F., and Hopkins, M. A.: A conceptual model for pancake-ice formation in a wave field, Annals of Glaciology, 33, 361-367, 2001.

Smith, M., Stammerjohn, S., Persson, O., Rainville, L., Liu, G., Perrie, W., Robertson, R., Jackson, J., and Thomson, J.: Episodic reversal of autumn ice advance caused by release of ocean heat in the Beaufort Sea,

575 Journal of Geophysical Research: Oceans, 123, 3164-3185, 2018.

Smith, M., and Thomson, J.: Ocean surface turbulence in newly formed marginal ice zones, Journal of Geophysical Research: Oceans, 124, 1382-1398, 2019.

Snyder, R. L., Dobson, F. W., Elliott, J. A., and Long, R. B.: Array measurements of atmospheric pressure fluctuations above surface gravity waves, Journal of Fluid mechanics, 102, 1-59, 1981.

580   Squire, V. A., Dugan, J. P., Wadhams, P., Rottier, P. J., and Liu, A. K.: Of ocean waves and sea ice, Annual
        Review of Fluid Mechanics, 27, 115-168, 1995.

        Squire, V. A.: Of ocean waves and sea-ice revisited, Cold Regions Science and Technology, 49, 110-133,
        2007.

        Squire, V. A.: A fresh look at how ocean waves and sea ice interact, Philosophical Transactions of the Royal
585   Society A: Mathematical, Physical and Engineering Sciences, 376, 20170342, 2018.

        Stopa, J. E., Ardhuin, F., Chapron, B., and Collard, F.: Estimating wave orbital velocity through the azimuth
        cutoff from space-borne satellites, Journal of Geophysical Research: Oceans, 120, 7616-7634, 2015.

        Stopa, J., Ardhuin, F., Thomson, J., Smith, M. M., Kohout, A., Doble, M., and Wadhams, P.: Wave
        attenuation through an Arctic marginal ice zone on 12 October 2015: 1. Measurement of wave spectra and
590   ice features from Sentinel 1A, Journal of Geophysical Research: Oceans, 123, 3619-3634, 2018a.

        Stopa, J. E., Sutherland, P., and Ardhuin, F.: Strong and highly variable push of ocean waves on Southern
        Ocean sea ice, Proc Natl Acad Sci U S A, 115, 5861-5865, 10.1073/pnas.1802011115, 2018b.

        Stroeve, J., Holland, M. M., Meier, W., Scambos, T., and Serreze, M.: Arctic sea ice decline: Faster than
        forecast, Geophysical research letters, 34, 2007.

595   The WAVEWATCH III® Development Group (WW3DG): User manual and system documentation of
        WAVEWATCH III® version 6.07. Tech. Note 333, NOAA/NWS/NCEP/MMAB, College Park, MD, USA,
        465 pp. +Appendices, 2019.

        Thomson, J., Ackley, S., Girard-Ardhuin, F., Ardhuin, F., Babanin, A., Boutin, G., Brozena, J., Cheng, S.,
        Collins, C., Doble, M., …, and Wadhams, P.: Overview of the arctic sea state and boundary layer physics
600   program, Journal of Geophysical Research: Oceans, 123, 8674-8687, 2018.

        Wadhams, P., Squire, V. A., Goodman, D. J., Cowan, A. M., and Moore, S. C.: The attenuation rates of ocean
        waves in the marginal ice zone, Journal of Geophysical Research: Oceans, 93, 6799-6818, 1988.

        Wang, R., and Shen, H. H.: Experimental study on surface wave propagating through a grease–pancake ice
        mixture, Cold Regions Science and Technology, 61, 90-96, 2010a.

605   Wang, R., and Shen, H. H.: Gravity waves propagating into an ice-covered ocean: A viscoelastic model,
        Journal of Geophysical Research: Oceans, 115, 2010b.

        Weeks, W. F., and Assur, A.: The mechanical properties of sea ice, COLD REGIONS RESEARCH AND
        ENGINEERING LAB HANOVER NH, 1967.

        Zhao, X., and Shen, H. H.: Wave propagation in frazil/pancake, pancake, and fragmented ice covers, Cold
610   Regions Science and Technology, 113, 71-80, 2015.